Bulletin of Volcanology (2023) 85:18
https://doi.org/10.1007/s00445-023-01633-4

RESEARCH ARTICLE

Years of magma intrusion primed Kīlauea Volcano (Hawai'i) for the 2018 eruption: evidence from olivine diffusion chronometry and monitoring data

Adrien J. Mourey[1] · Thomas Shea[1] · Fidel Costa[2,3,4] · Brian Shiro[5] · Ryan J. Longman[6]

Received: 22 August 2022 / Accepted: 8 February 2023 / Published online: 28 February 2023

Abstract

The mechanisms that led to the exceptionally large Kīlauea 2018 eruption are still poorly understood and actively debated. External processes such as rainfall events or flank sliding have been proposed to play a triggering role. Here, we present field, geophysical, and petrological observations to show that internal changes within the magmatic plumbing system most likely led to the eruption. Chemical zoning in olivine crystals records the intrusion of primitive magma that is concurrent with deep seismicity and inflation at the volcano's summit. Magma replenishment and pressurization of the summit reservoirs already started around 2014 and accelerated towards the eruption. Kīlauea volcano was therefore primed to experience a shift in eruptive activity in 2018. This pressure increase associated with reservoir replenishment may have been sufficient to overcome a previously blocked conduit. These findings imply that precursory signs of years of protracted magma intrusion and pressurization of the system may be recognizable in the future, which could lead to improved hazards mitigation.

Keywords Olivine · Fe-Mg diffusion · Bottom-up trigger · Kīlauea Volcano

Introduction

Understanding the processes that lead to volcanic eruptions is among the most pressing challenges of volcanology (e.g., Sparks 2003; Burchardt et al. 2022; Dietterich and Neal 2022). Magmatic processes, such as ascent (Ruprecht and Plank 2013) and intrusion (Costa and Chakraborty 2004), can prime a volcanic system for eruption days to years prior. Systems that are primed to erupt can ultimately be triggered by external events such as flank collapse or glacier melting (Sigvaldason et al. 1992) or internal processes such as reservoir overpressure (Neal et al. 2019). Further adding to the challenge is the observation that volcanoes are complex systems and their eruptive dynamics can result from the combined interaction between tectonics, hydrothermal activity, magma plumbing system, and factors external to the volcano such as moon and sea tides, or weather patterns (e.g., Schmincke 2004; Aubry et al. 2022; Marshall et al. 2022). Given the large number of interacting parameters, it is often difficult to identify the ultimate trigger of a given eruption. However, important clues can be gathered by investigating the location and duration of precursory magmatic events (Sparks 2003).

Editorial responsibility: M.R. Patrick

This paper constitutes part of a topical collection: The historic events at Kīlauea Volcano in 2018: summit collapse, rift zone eruption, and Mw6.9 earthquake

✉ Adrien J. Mourey
amourey@hawaii.edu

[1] Department of Earth Sciences, University of Hawai'i at Mānoa, Honolulu, HI, USA

[2] Asian School of the Environment, Nanyang Technological University, Singapore, Singapore

[3] Earth Observatory of Singapore, Nanyang Technological University, Singapore, Singapore

[4] Institut de Physique du Globe de Paris, Université Paris Cité, CNRS, Paris, France

[5] U.S. Geological Survey Hawaiian Volcano Observatory, Hilo, HI, USA

[6] East-West Center, Honolulu, HI, USA

Geophysical observations such as seismicity and deformation can be used to infer the location and progression of magma movement (Sparks 2003). The type of seismicity (i.e., very long period, high frequency) can be used to diagnose reservoir pressurization, wall-rock fracturing, presence of magma or fluid, or volcano flank slip (e.g., Sparks 2003; Roman and Cashman 2006; Gudmundsson et al. 2022). Despite these observations, however, it is often difficult to make unambiguous interpretations about the underlying processes and mechanism of the signals that are measured. For example, is the seismicity caused by magma advection and recharge (Albert et al. 2019), a transmitted pressure pulse (Gudmundsson et al. 2022), or volcano-tectonic events (Sparks et al. 2003). Complementary information on the processes occurring in volcanic plumbing systems can be gathered by studying the chemical characteristics of crystal cargo erupted with the magma (e.g., Ruprecht and Plank 2013; Lynn et al. 2017a; Mourey et al. 2023). Compositional changes recorded in crystals have thus been increasingly leveraged to characterize the magmatic processes leading to eruption and their timescales, such as recharge/mixing (Costa and Chakraborty 2004), mush remobilization (Albert et al. 2019), rapid magma ascent (Ruprecht and Plank 2013), cooling (Newcombe et al. 2014), and magma reservoir assembly (Cooper and Kent 2014). Integrating field, geophysical, and petrological records therefore increase our likelihood of successfully identifying the nature and location of eruption priming and triggering agents.

Kīlauea 2018 eruption summary

The 2018 lower East Rift Zone (LERZ) eruption of Kīlauea marked an important change in the volcano’s behavior. An abrupt increase in inflation rates was recorded by tiltmeters and GPS stations at the summit and upper East Rift Zone in April 2018, which prompted the Hawaiian Volcano Observatory to issue warnings that a change in eruptive activity was a possible outcome (Neal et al. 2019). The Pu‘u‘ō‘ō vent, active between 1983 and 2018, collapsed on 30 April 2018. Combined seismic and deformation data showed that, between 30 April and 3 May, magma was injected into the LERZ ~20 km East of Pu‘u‘ō‘ō (Fig. 1), a region that had not seen significant magma input since 1960 (Neal et al. 2019; Sigmundsson 2019). The first eruptive fissures opened in the Leilani Estates subdivision on 3 May. The first 2 weeks of eruption occurred along 24 fissures with evolved basaltic and andesitic bulk compositions (Fig. 2; Gansecki et al. 2019), and evolved basaltic and dacitic glasses (fissure 17; Wieser et al. 2022), not observed in prior historical eruptions. Activity shifted around 16 May to steadier fountaining of progressively more mafic magma. This transition marked the arrival of a mafic olivine-bearing magma (matrix glass with MgO ~ 4.9–7.2 wt.%). Between the end of May and 4 August, activity focused on fissure 8 (Ahu‘ailā‘au), effusion rates increased to above 100 m^3/s (Patrick et al. 2019a; Anderson et al. 2019; Dietterich et al. 2021), and channelized lava was transported >10 km to the ocean. The eruption waned

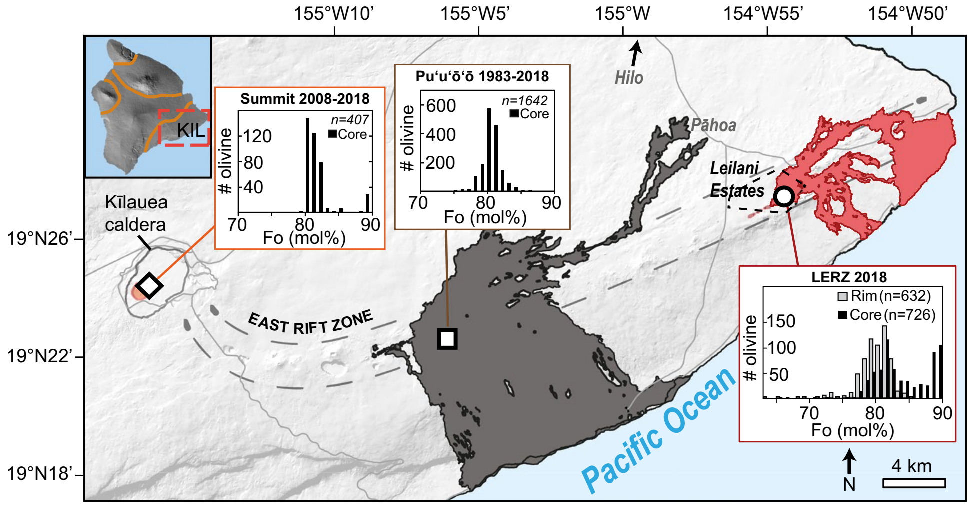

Fig. 1 Map of Kīlauea Volcano on the Island of Hawai‘i (modified after Mourey et al. 2022). The location of recent eruptions (summit lava lake, Pu‘u‘ō‘ō and the 2018 LERZ eruption). The olivine compositions were compiled from the literature (Mourey et al. 2022) and this study with ‘*n*’ the number of olivine analyzed. Olivine compositions from the summit Halema‘uma‘u overlook are bimodal with a statistically higher proportion of $Fo_{80–82}$ (~90% of all olivine analyzed) and a lower proportion of Fo_{89}. Pu‘u‘ō‘ō olivine compositions are restricted to $Fo_{78–83}$. Olivine core compositions from the 2018 LERZ eruption are bimodal with the same proportion of $Fo_{88–89}$ and $Fo_{80–82}$ olivine. A significant proportion (~15%) of the olivine with $Fo_{84–87}$ measured in 2018 are uncommon at the summit lava lake and Pu‘u‘ō‘ō

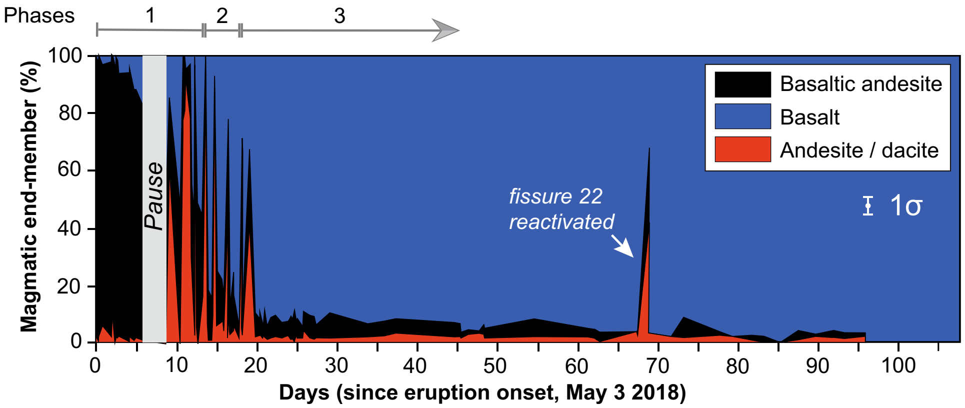

Fig. 2 Contribution (by mass) of the three main magma end-members over the course of the eruption. Olivine basalt largely dominates during the phase 2 and 3. End-member percentage was calculated based on TiO_2-K_2O relationships from whole-rock compositions (Gansecki et al. 2019; Pietruszka et al. 2021)

abruptly after 4 August, with the end of summit collapse (Neal et al. 2019). Light spattering was observed until 5 September at fissure 8. Long-period earthquake swarms started 6 months prior to the eruption at ~5–13-km depth below sea level, below the South Caldera reservoir (Flinders et al. 2020), and support the pressurization of the summit system (mainly the 3–5-km-deep South Caldera reservoir and possibly the ~1-km-deep Halemaʻumaʻu reservoir; Wieser et al. 2021; Lerner et al. 2021a). A deeper crustal reservoir, suggested to exist during the Keanakākoʻi tephra period (Lynn et al. 2017a; Mourey et al. 2022), cannot be completely ruled out, but there is currently no evidence for a sustained magma reservoir beneath the South Caldera reservoir (>5–6 km) and the region of deep seismicity (tremors between 30 and 60 km focused beneath the South West Rift Zone; Wech and Thelen 2015).

Even though the 2018 Kīlauea LERZ eruption was one of the best monitored volcanic crises to date (Neal et al. 2019; Gansecki et al. 2019), its underlying causes are currently debated (Neal et al. 2019; Farquharson and Amelung 2020). Seismic and deformation data suggest that the magmatic system was being pressurized starting early March 2018 in the middle to upper East Rift Zone (UERZ; Flinders et al. 2020; Olivier et al. 2019). By contrast, it was recently proposed that the increase of the groundwater pressure, caused by heavy rainfall in the months prior to May 2018, weakened the East Rift Zone and triggered the eruption (Farquharson and Amelung 2020). To better understand the circumstances leading up to eruption, we reconstruct the timeline of pre-2018 magmatic events using timescales recovered from Fe-Mg-Ni-Ca diffusion modeling in olivine. Results from our petrologic investigation are then integrated with seismicity and deformation and compared against other proposed eruption priming and triggering mechanisms. Decades of geophysical and petrological monitoring data (Poland et al. 2014; Thornber et al. 2015; Patrick et al. 2015) and radiogenic isotope data from previous eruptions (Pietruszka et al. 2018) provide essential context to understand the magmatic processes leading to 2018.

Methods

Electron Probe analyses

Si, Mg, Fe, Ca, and Ni concentrations in olivine cores and rims from all samples were measured using a 20-keV accelerating voltage and a 200-nA beam current with a diameter of 10 µm. A beam diameter of 3 µm was used for olivine transects. Peak counting time was 40 s for each element. Olivine san Carlos USNM 111312/444 was used as internal standard for Si and Mg, CalTech Ni-ol for Ni, and the Kakanui Augite USNM 122142 for Ca. Olivine UNSM Springwater 2566 was used as an external standard to check for drift. Relative precision (2σ) based on repeat analysis of olivine Springwater standard is better than 1% for Si, Fe, and Mg and <5% for Ca and Ni. Accuracy is better than 1% for all elements (see supplementary data).

For glass analyses, an accelerating voltage of 15 keV, a current of 10 nA, and a beam diameter of 10 µm were used. On-peak count times were 30 s (Si, Ti, Fe, Mn, Ca, Na, P) or 70 s (Al, Mg, K). A99 basalt glass (USNM 113498/1) was used for Si, Al, Fe, Mg, and Ca; Sphene glass for Ti; Verma garnet for Mn; Amelia albite for Na; Orthoclase (OR-1) for K; and fluor-apatite (USNM 104021) for P. VG-2 was used as an external standard and re-analyzed regularly to monitor any potential drift. Relative precision (2σ) based on repeat analyses of VG-2 standard is better than 1% for Si, Al, Fe, Mg, and Ca; about 2% for Na; 3% for Ti; 4% for K; 11% for Mn; and 15% for P. Accuracy is <1% for Si, Al, Mg, Ca, Na, and K; about 2% for Ti, Fe, and P; and 5% for Mn.

Diffusion equations

Mixing-to-eruption timescales were obtained by modeling element diffusion profiles measured between the edge and core of olivine crystals from 6 samples erupted at the LERZ during phase 3 of the 2018 eruption (Gansecki et al. 2019). The diffusion simulations were performed using a forward model incorporating the finite difference method (e.g., Costa et al. 2008). The olivine/melt boundary was considered open to the melt, which acts as an infinite reservoir of Fe-Mg. Olivine rim compositions were held constant. The location of the profiles was carefully chosen perpendicular to crystal faces and away from corners to avoid 3D sectioning effects (Shea et al. 2015a). We performed 1D numerical models for each olivine crystal using the concentration-dependent version of Fick's second law (Costa et al. 2008):

$$\frac{\partial C_{\mathrm{i}}}{\partial t} = \frac{\partial}{\partial x}\left(D_{\mathrm{i}}\frac{\partial C_{\mathrm{i}}}{\partial x}\right) \tag{1}$$

with C_{i} the concentration in Mg-Fe in the olivine, x the distance from the edge (μm), and D_{i} the diffusion coefficient (in m^2/s), with the Fe-Mg diffusion in olivine calculated along the *c*-axis (Dohmen and Chakraborty 2007) defined as

$$D_c^{\mathrm{Fe-Mg}} = 10^{-9.21}\left(\frac{fO_2}{10^{-7}}\right)^{1/6} 10^{3\left(X_{\mathrm{Mg}}-0.9\right)} \exp\left(-\frac{201{,}000 + \left(P - 10^5\right).7 \times 10^{-6}}{RT}\right) \tag{2}$$

with P the pressure (fixed at 60 MPa in our models, corresponding to the estimated pressure in the summit reservoirs), T is the temperature in K, R is the gas constant in $\mathrm{J \cdot mol^{-1} \cdot K^{-1}}$, and fO_2 is the oxygen fugacity calculated to track the QFM buffer (Zolotov and Fegley 1999) with

$$fO_2 = 10^{(8.912-(25{,}160/T))} \text{ in Pa} \tag{3}$$

Model temperatures were estimated using Fe-Mg partitioning relationships between olivine and the mafic melt. Olivine was added to the glass composition until reaching equilibrium ($K_{\mathrm{D}}^{\mathrm{Fe^{2+}-Mg}} = 0.33$; Shea et al. 2022; Putirka 2016). We fixed $\mathrm{Fe^{3+}/Fe_T} = 0.18$ (Moussallam et al. 2016; Helz et al. 2017). We then calculated the temperature using the MgO-glass thermometer of Shea et al. (2022). The standard deviation in this regression is 12 °C; therefore, 2σ = 24 °C. This uncertainty has been combined with the uncertainty in the $K_{\mathrm{D}}^{\mathrm{Fe^{2+}-Mg}}$ for the final temperature used in the diffusion models. Because diffusion of Fe-Mg in olivine is anisotropic, diffusivity along the profile D_{profile} was calculated using

$$D_{profile} = D_a(\cos\alpha)^2 + D_b(\cos\beta)^2 + D_c(\cos\gamma)^2 \tag{4}$$

with α, β, and γ as angles between measured profile and *a*-, *b*-, and *c*-axes, and $6D_a = 6D_b = D_c$ (Costa and Dungan 2005). The orientation of the olivine sections was obtained using Electron Backscatter Diffraction (EBSD) patterns on a JEOL 5900 Scanning Electron Microscope at the University of Hawai'i.

The mixing-to-eruption timescale corresponds to the best fit of all modeled curves with the data using the root-mean-square method (Girona and Costa 2013). The uncertainty in pressure in our models induced into timescales using a pressure of 50 MPa (mixing in the upper Halema'uma'u reservoir) or 100 MPa (in the deeper South Caldera reservoir) represents time uncertainties of around 2% in the models. The uncertainty from potential variations in fO_2 associated with different estimates for Kīlauea magmas, from QFM 0 to QFM + 0.7 (Lerner et al. 2021b), yields to a 22% decrease in mixing-to-eruption timescales.

We distinguished two olivine zoning histories based on core and rim compositions. A first olivine population records one diffusion event after mixing of a primitive magma at equilibrium with $\mathrm{Fo_{86–89}}$ with the main $\mathrm{Fo_{80–82}}$ magma, and possibly a very minor $\mathrm{Fo_{84}}$ magma from the summit reservoirs. This mixing-to-eruption timescale is called 't_1.' The second olivine population records two mixing events: mixing at the summit t_1 before the eruption and an additional syn-eruptive mixing with the stored high-Ti basalt from the LERZ in equilibrium with $\mathrm{Fo_{72–77}}$. As detailed below, simulations were performed iteratively for each crystal to estimate the best location of the initial and boundary conditions for both diffusion events.

Boundary conditions and starting concentration

We considered open boundaries for diffusion modeling, where the concentration at the rim remains fixed. Models are isothermal but different temperatures were chosen for the first step of diffusion (t_1) and the second step (t_2). The assumption of constant temperature after magma mixing holds particularly well because (1) the summit reservoirs in which the high-Fo olivine-bearing magmas intruded have been remarkably steady in composition (MgO content and Fo; Poland et al. 2014) over the decade prior to 2018 (see supplementary material). Times series of glass MgO, olivine Fo, and eruption temperature over the decade prior to 2018 show that thermal fluctuations in the period relevant to our diffusion timescales are minor; (2) The volume of intruding recharge magma is generally small relative to the overall volume of Kīlauea's summit reservoirs (South Caldera is 3–20 km^3 and Halema'uma'u is 1–10 km^3; Poland et al. 2014). Only the largest inputs of primitive magma have been recorded by lava MgO content in the two decades prior to 2018, the last important one occurring in 2007 (Poland et al. 2014; Olivier et al. 2019). The rim composition (and by association, temperature) for t_1 is selected based on the core and rim compositions of the olivine population as a whole rather than adapted/modified significantly for each individual crystal. In cases where there was evidence for an additional intermediate step (i.e., $\mathrm{Fo_{84}}$), the choice of rim composition was based on the occurrence of other olivine crystals with these intermediate compositions either at the core or rim, and/or on the impossibility of properly fitting a one-step model. The end-member compositions and boundary conditions used for most models ($Fo_{87–89}$, Fo_{84}, $Fo_{80–82}$, and $Fo_{72–77}$) are well justified based on olivine rim populations and prior studies (Gansecki et al. 2019). The least well represented end-member (Fo_{84}) is mainly seen in one sample and consists in ~15% of our t_1 timescales. For the olivine that mixed with the high-Ti basalt in the East Rift Zone (rims with $Fo_{73–77}$), the starting concentration for the first step of diffusion was fixed at $Fo_{80–82}$ and the second starting concentration for the second step of diffusion was fixed at $Fo_{73–77}$ (Fig. 3). We chose to model some of the profiles in two steps if the best fit of a one-step diffusion model in Fo, Ni, or Ca could not adequately reproduce the data. We define the boundary condition of the first step of diffusion based on the olivine compositions recorded at the Kīlauea summit (in equilibrium with $Fo_{80–82}$ and possibly with Fo_{84}). For the first step t_1, the exact position of the

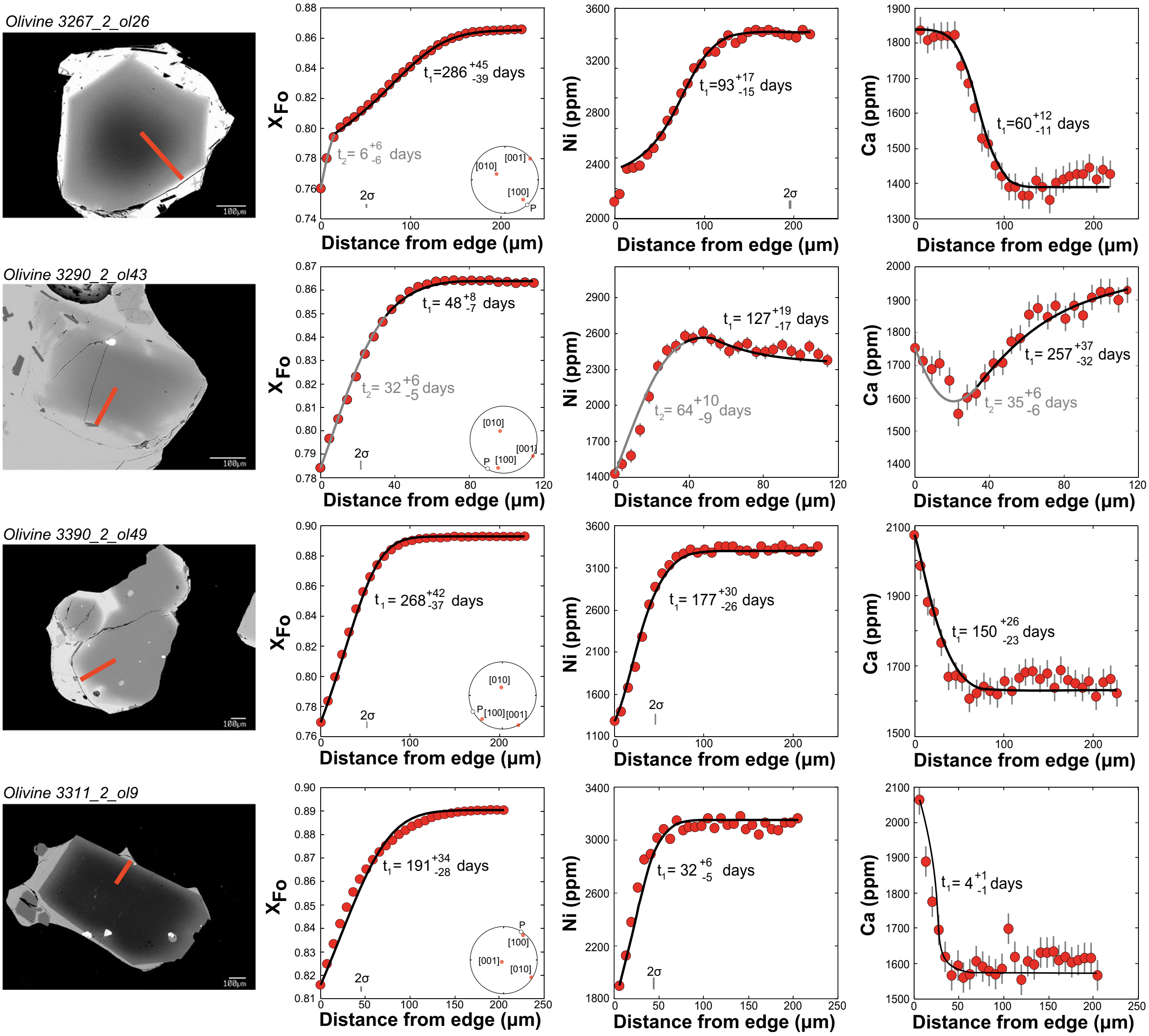

Fig. 3 **Data and diffusion model best fits for olivine crystals erupted during phases 2 and 3 of the 2018 eruption**. Backscattered electron (BSE) image of the analyzed olivine crystal with the location of the EPMA profile (red line), EPMA profile of mole fraction forsterite content (X_{Fo}), Ni and Ca contents shown in red. Inset is an equal area pole figure of the crystal showing the orientation of the main crystallographic axes (red points) relative to the profile (white point marked '*P*'). An additional diffusion step t_2 is necessary to fit some profiles and is consistent with the different olivine populations identified in the general core-rim data. Mixing-to-eruption timescales t_1 and t_2 correspond here to mixing prior to the eruption at the summit

rim is found iteratively: a suitable rim position is found when Ca, Ni, and Fe-Mg profiles are all well fit by a diffusion model that uses the same initial rim position. For the second step t_2, the gradients and lower Fo rims (rim here just denotes the outside most part of the crystal, not necessarily a large overgrowth) are fairly thin; it is often difficult to assess whether a rim grew or not. Any rim growth prior to the diffusive event t_2 would only act to shorten the t_2 timescales obtained by a small amount.

Choice of elements for diffusion modeling

Analytical profiles include Fe, Mg, Ni, and Ca analyses (Fig. 3). All these elements can be used for diffusion modeling (Costa and Dungan 2005; Ruth et al. 2018). However, Fe-Mg interdiffusion is by far the best constrained in terms of number of experiments used to calibrate the expressions (Dohmen and Chakraborty 2007; Chakraborty 2010). While we also carried out diffusion modeling for Ni and Ca, we focus on Fe-Mg timescales, which are more accurate. Overall, the durations extracted from the three elements compare favorably, but Ca and Ni timescales tend to be systematically shorter than Fe-Mg values (Fig. 4). The underprediction of Ca or Ni over Fe-Mg is, in fact, a relatively common observation (Lynn et al. 2017b; Ruth et al. 2018) most likely associated with the lower accuracy of diffusivity data for Ca and Ni (Gordeychik et al. 2020), rather than a problem of precision within experimental diffusivity data or temperature (Coogan et al. 2005; Costa et al. 2020).

Geophysical monitoring

Seismicity

The geographic boundaries of the summit seismicity are as follows: [19.35, 19.44] latitude/[−155.304, −155.2] longitude (see supplementary material). We considered all magnitude earthquakes in the Hawaiian Volcano Observatory seismic catalog from 1 January 2010 to 30 April 2018 between 5- and 13-km depth below sea level.

GPS displacement

We selected three GPS stations (HOVL, UWEV, and OUTL) to track the vertical and northward displacement of the summit area.

Modeling of diffusion- vs. growth-induced zoning of olivine

Previous studies have shown that growth- and diffusion-induced compositional zoning can be distinguished by using multiple elements that diffuse at different rates and/or have different levels of compatibility during crystallization (Costa and Dungan 2005; Costa et al. 2008; Shea et al. 2015b). For the present work (Fig. 5), a 3D Fo and Ni diffusion model with a realistic morphology (olivine elongated along the *c*-axis; Mourey and Shea 2019) and incorporating the effects of *T*, *P*, fO_2, and anisotropy in the diffusivity calculations was carried out numerically

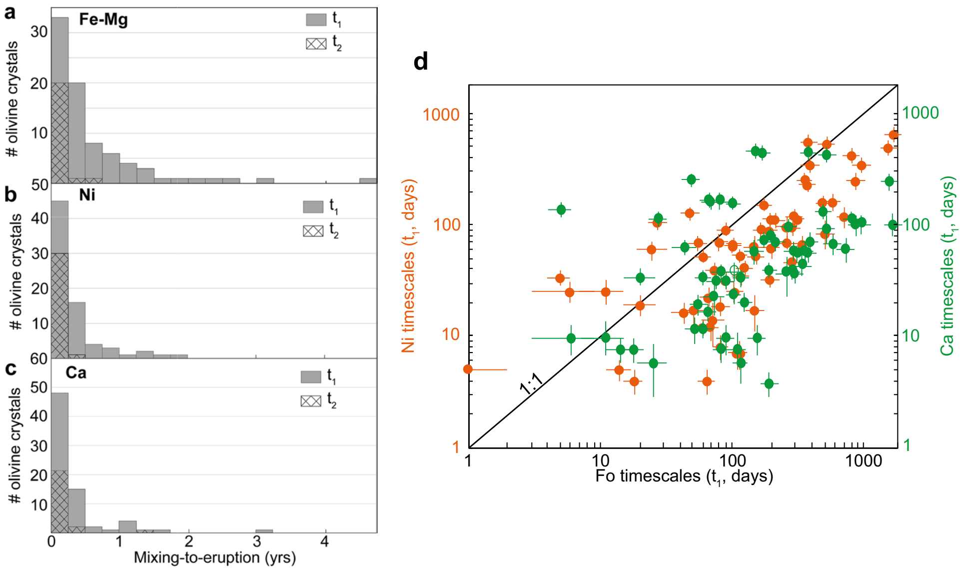

Fig. 4 **Fe-Mg, Ni, and Ca mixing-to eruption timescales. a Fe-Mg timescales**. **b** Ni timescales. **c** Ca timescales. 't_1' represents pre-eruptive mixing and 't_2' is syn-eruptive mixing with stored magma at the lower East Rift Zone. **d** Comparison Fo vs. Ni vs. Ca timescales. The error bars correspond to the uncertainty on the timescales

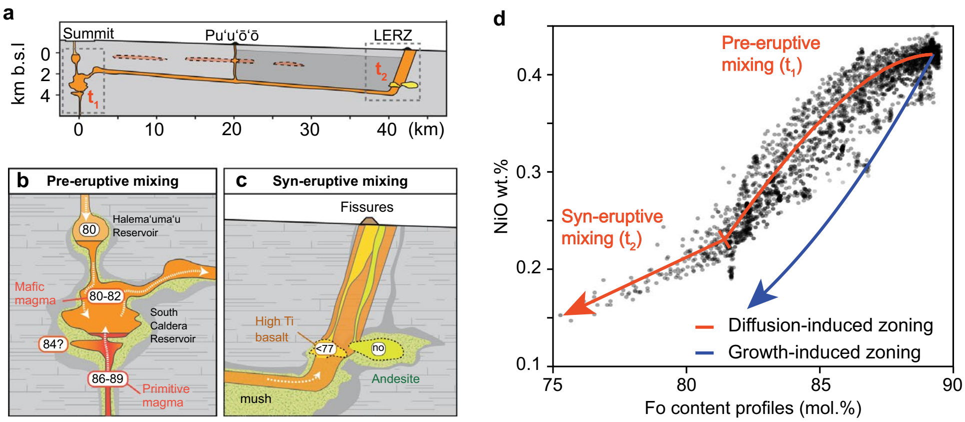

Fig. 5 **Pre-eruptive and syn-eruptive mixing during the 2018 Kīlauea eruption**. **a** Cross section through the Kīlauea magmatic system showing the location of the pre-eruptive (t_1) and syn-eruptive (t_2) mixing and the depth below sea level (km b.s.l.) of the main reservoirs (Poland et al. 2014) and lower East Rift Zone melt pockets (Wieser et al. 2022). **b** Pre-eruptive mixing of melts in equilibrium with $Fo_{86–89}$ (crustal recharge melts) and melts in equilibrium with $Fo_{80–82}$ (reservoir melts). **c** Syn-eruptive mixing in the lower East Rift Zone with stored evolved basaltic melts in equilibrium with $Fo_{<77}$ olivine. Numbers correspond to the Fo content in equilibrium with the melt (the mention 'no' means that no olivine was found in the andesite erupted at fissure 17). **d** Distinguishing crystal growth from diffusive relaxation in LERZ olivine. Ni and Fo concentrations measured along analytical transects within 71 olivine crystals (6 samples collected between 24 May and 5 August 2018). The crystallization trend was modeled using an initial MgO = 14.5 wt%, fO_2 along the QFM buffer, and T = 1350 °C. Fe-Mg and Ni zoning in LERZ 2018 olivine follow a concave up 'diffusion trend' (t_1 profiles), and a linear trend at lower Fo, also interpreted as diffusion

using Fe-Mg-Ni diffusivities in olivine (Dohmen and Chakraborty 2007; Chakraborty 2010) and methods previously published (Shea et al. 2015b). Initial and final Fo and Ni concentrations were chosen to broadly match the compositions of Fo_{89} olivine cores. Temperature was calculated from the rim composition ($Fo_{75–84}$). In parallel, we modeled fractional crystallization of a 2018-like parental melt using our own codes (first developed by Lynn et al. (2017a)) given that MELTS (Gualda et al. 2012) and Petrolog3 (Danyushevsky and Plechov 2011) do not incorporate some of the partitioning models that we prefer for Kīlauea lavas. A starting melt composition was selected based on post-entrapment-corrected primitive LERZ 2018 melt inclusion compositions (Table 1). The starting magma has FeO = 11 wt.% and MgO = 14.4 wt.%, and is similar to melt inclusion compositions reported in Sides et al. (2014) or Lerner et al. (2021a). The initial NiO content in the melt was set to 0.061 wt.% so that the first crystallizing olivine would have a NiO composition similar to the maximum NiO measured in the 2018 Fo_{89} olivine (NiO ~0.43 wt.%; Fig. 5). Fe-Mg equilibrium at each crystallization increment was dictated by the exchange coefficient $K_D^{Fe^{2+}-Mg}$ = 0.33 (Shea et al. 2022; Putirka 2016) and D_{Mg} was calculated based on Putirka (2008). Fe^{2+}/Fe^{3+} was calculated based on the model of Kress and Carmichael (1991) for fO_2 conditions at the QFM buffer. D_{Ni} was calculated based on Matzen et al. (2013). We chose a pressure P = 80 MPa, within the depth range corresponding to the deeper summit reservoir, but note that P has little effect on the resulting fractional crystallization path. The model was stopped at a temperature of 1170 °C, right before plagioclase and clinopyroxene come into the crystallizing assemblage (Helz and Thornber 1987).

Table 1 Starting and final melt composition used for the crystallization model

wt.%	Starting melt	Final melt
SiO_2	49.11	51.17
TiO_2	1.94	2.35
Al_2O_3	11.09	13.48
Fe_2O_3	0.00	0.00
FeO	10.94	10.48
MnO	0.14	0.14
MgO	14.42	7.48
CaO	9.80	11.85
Na_2O	2.04	2.48
K_2O	0.32	0.39
P_2O_5	0.15	0.18
NiO	0.06	0.01
Total	100	100

Compositional zoning in olivine during fractional crystallization (growth-induced zoning)

In this section, we provide further details on the calculations performed to determine the composition of olivine within a melt undergoing fractional crystallization.

The initial melt (Table 1) and olivine compositions are chosen based on high-Fo (Fo_{89}) olivine and their corrected host melt inclusion compositions

A relationship between temperature and fraction of olivine crystallized was obtained by using MELTS (Gualda et al. 2012) with the initial melt composition as an input, and fitting a second-order polynomial ($R^2 > 0.95$):

$$x_{ol} = -1.399 \times 10^{-4} T^2 + 0.245T - 75.785 \tag{5}$$

with T in °C. MELTS predicts an olivine liquidus temperature of 1354 °C for this composition.

Crystallization was then modeled as small temperature steps (1 °C) and corresponding crystallization increments using normal mass balance for each element/oxide:

$$C_L^{new} = \frac{C_L^{old}}{D_{S/L}^{new} \times dx_{ol} + \left(1 - dx_{ol}\right)} \tag{6}$$

where dx is the crystal fraction increment, C_L is the melt composition, and D is the partition coefficient for a given element between olivine and melt. Note that this equation is typically used for equilibrium crystallization, but used here for small increment fractional crystallization where olivine and melt are not allowed to re-equilibrate.

The corresponding solid composition at each step is simply

$$C_S^{new} = D_{S/L}^{new} \times C_L^{new} \tag{7}$$

The partition coefficients for Fe-Mg and Ni are recalculated at each increment as follows:

- D_{Ni} is calculated using the formulation of Matzen et al. (2013):

$$\ln\ D_{Ni}^{molar} = -\frac{\Delta_r H^{\circ}_{T_{ref},P_{ref}}}{RT} + \frac{\Delta_r S^{\circ}_{T_{ref},P_{ref}}}{R} - \ln\left(\frac{X_{MgO}^{liq}}{X_{MgSi_{0.5}O_2}^{ol}}\right) \tag{8}$$

with

$$-\frac{\Delta_{\mathrm{r}} H^{\circ}_{\mathrm{T_{ref},P_{ref}}}}{R} = 4338\ K \text{ and } \frac{\Delta_{\mathrm{r}} S^{\circ}_{\mathrm{T_{ref},P_{ref}}}}{R} = -1.956 \tag{9}$$

- D_{Mg} is calculated using the formulation of Putirka (2008):

$$\ln\ D_{Mg}^{ol/liq} = -2.158 + 55.09\frac{P(GPa)}{T(^{\circ}C)} - 6.213 \times 10^{-2}\left[H_2O^{liq}\right] + \frac{4430}{T(^{\circ}C)} + 5.115 \times 10^{-2}\left[Na_2O^{liq} + K_2O^{liq}\right] \tag{10}$$

with a melt $H_2O = 0.5$ wt.% and $P = 80$ MPa, conditions relevant to magmas arriving in the summit reservoirs but that have little effect here on the partition coefficient calculated.

- D_{Fe} is calculated from D_{Mg} using an exchange coefficient $K_{\mathrm{D}}^{\mathrm{Fe^{2+}-Mg}} = 0.33$.
- D_{Si} is fixed and set at 0.78.

Because Fe-Mg partitioning between olivine and melt requires knowledge of iron speciation, we calculate melt Fe^{2+} and Fe^{3+} content using the formalism of Kress and Carmichael (1991). We opted for fO_2 conditions at the QFM buffer, consistent with recent estimates (Lerner et al. 2021a; Moussallam et al. 2019). The melt and olivine compositions were calculated during cooling over the temperature range T = 1360–1170 °C. Below this temperature, the melt becomes multiply saturated with clinopyroxene and plagioclase (Helz and Thornber 1987).

Re-examining correlations between eruptions and rainfall

We examined a recently proposed alternative mechanism, whereby extreme rainfall triggered the 2018 and other twentieth-century Kīlauea eruptions (Farquharson and Amelung 2020). We looked at the daily and monthly rainfall gauge records from the Hawai‘i Volcanoes National Park (HVNP) summit station (USC00511303) beginning in 1949 and ending in 2015. Rainfall gauge data does not encompass the 2018 eruption period or the period 1920–1949. To address the issues of data gaps in the instrumental record, we make use of several available resources to establish a complete 100-year record of monthly rainfall at the HVNP location. Prior to 1949, we use published monthly rainfall data (Frazier et al. 2016) and filled gaps in the historical record using spatial interpolation schemes (Eischeid et al. 2000). For post-2015 data, we first fill a daily rainfall time series using the Normal Ratio method (Longman et al. 2020). Then, the daily data undergoes quality control methods (Longman et al. 2018) and is finally aggregated to the monthly data series. To explore the rainfall-eruption relationship, we first examined the distribution of eruptions between 1920 and 2020 and monthly rainfall.

Regardless of whether rains are considered high or extreme over the 6-month period preceding the 2018 eruption, we next look at a possible correlation between eruptions and (1) well-known indicators of magmatic input to the plumbing system (tilt/deformation, increase in number of earthquakes per day) from the Wright and Klein (2014) compilation and, separately, (2) anomalously high rainfall. These relationships are critical to assess common eruption triggers, and to evaluate whether rainfall is an important consideration. If no clear temporal association between 6-month rainfall and eruption onset is found over the last century, then high pre-eruptive rainfall in 2018 becomes just as likely coincidental than correlated.

Results and discussion

We capitalize on the meticulous sampling of lavas carried out during the 2018 eruption (Gansecki et al. 2019) to study 11 samples collected from 7 May to 5 August. Olivine is present in all samples and was investigated for compositional zoning in Fe-Mg, Ni, and Ca. Olivine zoning shows that the crystals initially grew in a magma that was different in composition from their last carrier magma (Fig. 3). Diffusive re-equilibration between different compositional zones can therefore be leveraged to calculate timescales between the process causing compositional disequilibrium and eruption. Measuring multiple elements with different diffusivities like Fe-Mg and Ni can help distinguish the signatures of crystal growth- from diffusion-induced zoning (Costa et al. 2020). Olivine from the 2018 eruption is exclusively normally zoned, with characteristics of diffusion-controlled Fe-Mg and Ni zoning (Fig. 5). Chemical gradients in major and minor elements within the 2018 olivine are most likely associated with magma mixing (Lynn et al. 2017b). Normal zoning records two different mixing events. A first mixing event (t_1; Fig. 5) involved primitive melts (up to 14 wt.% MgO in post-entrapment crystallization corrected melt inclusions; Lerner et al. 2021a; Wieser et al. 2022) containing olivine with high-Fo cores (Fo$_{86–89}$) and a mafic magma (~7 wt.% MgO) at equilibrium with lower Fo olivine rims (Fo$_{80–82}$).

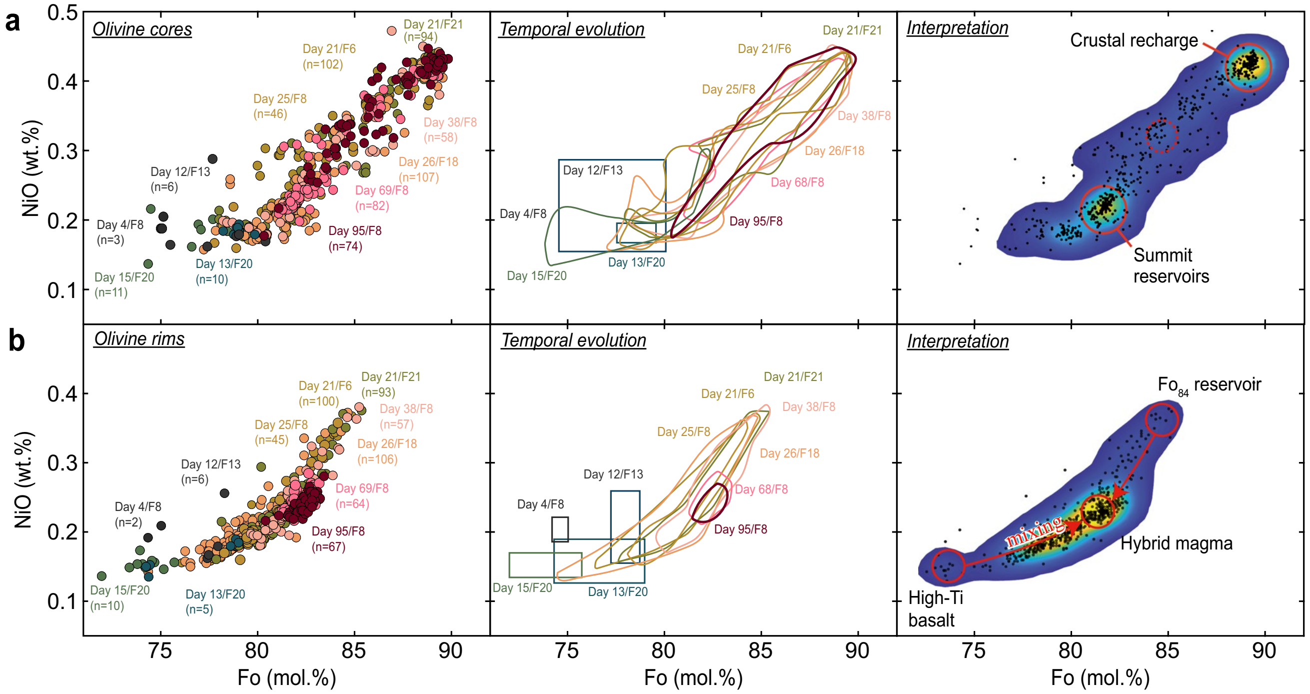

Fig. 6 Core and rim olivine compositions (Fo and NiO) in mafic lavas from the 2018 Kīlauea eruption. We report the date of formation of each sample, its location (fissure number, *F*), and the number of olivine analyzed (*n*). **a** Olivine core compositions highlight two magmatic end-members corresponding to primitive crustal recharges (Fo$_{89}$) and the resident summit magma (Fo$_{80–82}$). **b** Olivine rim compositions display three end-members: two poorly represented reservoirs with Fo$_{84}$ (of summit origin) and Fo$_{72–77}$ (magma stored in the LERZ) that mixed with the larger volume of magma stored and transported from the summit (Fo$_{80–82}$). The three clusters drawn in red (right panel) are based on the number of data points occupying this region in Fo-Ni and on the temporal evolution of the rim compositions (contours from the middle panel) during the eruption. Olivine rim compositions from the first 2 weeks of the eruption are represented with boxes due to the scarcity of olivine in the samples. The high-Fo$_{84}$ rim end-member is likely small but necessary to define the high Fo-Ni part of the plot. Rainbow colors in the right panel represent probability density contours (2D Gaussian smoothing kernel test) that highlight the more frequently occurring magmatic end-members

Mixing with the magma at equilibrium with $Fo_{80–82}$ led to the crystallization of variably thick rims (50 to 250 µm; see Supplementary Fig. 2) and the partial re-equilibration of these rims with the olivine core. This timescale t_1 corresponds to the time between the incorporation of variably high-Fo olivine into the summit reservoir(s) and eruption. The olivine cargo in question could represent populations crystallized over timescales of days (Mourey and Shea 2019) to centuries (Wieser et al. 2019) prior to the mixing event corresponding to t_1. A second mixing phase (t_2; Fig. 6a, c, and d) saw the magma containing the zoned olivine mix with an evolved basalt (bulk composition of ‘phase 1’ samples with 2.25–6.1 wt.% MgO; Gansecki et al. 2019). Little to no additional rim growth appears to have occurred during this stage. At equilibrium, this evolved phase 1 basalt would crystallize low-Fo rims ($Fo_{72–77}$).

Based on the timescales obtained for the first mixing event, we infer that the summit was being recharged and progressively pressurized since 2014, and that the priming of the system accelerated 6 months before the eruption. These findings differ from previous studies (Neal et al. 2019; Farquharson and Amelung 2020; Patrick et al. 2020); in that, we argue that the most important process in priming and triggering the eruption was ‘bottom-up’ (recharge) and not necessarily ‘top-down’ (sudden new blockage under the long-lived vent propagating to the summit or rainfall). A bottom-up priming model has important implications for monitoring the buildup of pressure and its acceleration.

Pre-eruptive magma mixing at the summit

Highly variable chemical zoning patterns in olivine crystals and heterogeneous melt compositions from prior Kīlauea eruptions have demonstrated that magma mixing occurs in both small ephemeral and larger summit reservoirs (Lynn et al. 2017b; Cashman and Edmonds 2019). High-Fo olivine (Fo_{89}) is most common in tephra from explosive summit eruptions (e.g., the Kulanaokuaiki and Keanakāko‘i tephra; Lynn et al. 2017a; Cashman and Edmonds 2019; Mourey et al. 2022), but are also present in lavas from a few past UERZ eruptions (Kīlauea Iki 1959, Maunaulu 1969–1974; Sides et al. 2014) and more distal events in the LERZ and the submarine Puna Ridge (Clague et al. 1995). High-Fo (Fo >86) olivine is in Fe-Mg equilibrium with primitive melts of MgO content ~14 wt.% and usually in disequilibrium with its carrier melt (Sides et al. 2014; Edmonds et al. 2015). The 2018 olivine core compositions suggest the presence of at least two end-member magmas, one in equilibrium with $Fo_{80–82}$ and the other with $Fo_{86–89}$ compositions (Fig. 7a and b). A small subset of cores and rims (<8%) also indicate the existence of a very minor Fo_{84} end-member. Our data does not allow us to say whether the primitive melts carried the $Fo_{86–89}$ olivine with them or whether those crystallized as those melts were close to or intruding the bottom of the South Caldera reservoir. Pietruszka et al. (2021) proposed an alternative hypothesis where phase 3 (Ahu‘ailā‘au, fissure 8) magma came from accumulated near-Pu‘u‘ō‘ō magma in the East Rift zone, but trace elements in olivine show that little Pu‘u‘ō‘ō magma made it to fissure 8 (Mourey et al. 2022). Fe-Mg-Ni-Ca chemical gradients in high-Fo olivine crystals erupted in 2018 in the LERZ imply a contact with Mg-rich (>13 wt.% MgO) melts the years preceding the eruption, and therefore refutes the hypothesis that old Pu‘u‘ō‘ō magmas supplied the 2018 LERZ eruption or the possibility that an active magma reservoir in the LERZ supplied the 2018 LERZ eruption (since no intrusion of Mg-rich melts occurred in the LERZ since at least the last eruption in 1960). $Fo_{86–89}$ olivine likely originates from parts of the summit reservoir system rather than from the deep East Rift Zone given that (1) seismicity and deformation were high at the summit but low within the ERZ in the year preceding the eruption indicating that intrusion of magma in the deep rift zone prior to 2018 is unlikely, (2) the high-Fo olivine does not exhibit the typical indicators of old rift cumulates (e.g., kink bands; Gansecki et al. 2019), and (3) any high-Fo olivine from older ERZ intrusions would have lost their high-Fo core via diffusion (Thomson and Maclennan 2013; Mourey et al. 2023). We considered alternative hypotheses for the origins of Fo_{89} olivine (see supplementary material) but none were fully consistent with the simple normal zoning, olivine morphologies (fully faceted), or absence of cumulate textures. Modeling diffusion from the Fo zoning profiles gives mixing-to-eruption timescales that range from <10 days to 4.5 years, recording mixing events back to 2014 (t_1; Fig. 7a and b). Pre-eruptive mixing recorded in olivine from the early samples from the phase 3 are generally more restricted in range and occurred more recently (most of them during the year preceding the eruption; Fig.7b) than the mixing-to-eruption timescales from late phase 3 olivine. By contrast, some of the olivine from the end of the eruption were in contact with $Fo_{80–82}$ melts (and crystallized $Fo_{80–82}$ rims) up to 4.5 years before the eruption (Fig. 7a). Recharge episodes older than 5 to 10 years prior to 2018 would have their high-Fo cores largely re-equilibrated to lower Fo content with the $Fo_{80–82}$ summit system (for a given olivine crystal size; Thomson and Maclennan 2013; Mourey et al. 2023), so that olivine crystals would not preserve timescale information.

Primitive melts in equilibrium with $Fo_{86–89}$ olivine compositions likely entered the South Caldera reservoir (Fig. 5), where they mixed with melts in equilibrium with $Fo_{80–82}$ olivine at different periods, starting in 2014. Injections of primitive magma were not large enough to be detected as significant changes in glass compositions in the last few years (Gansecki et al. 2019), but are preserved in the olivine cargo. The cumulative distribution of mixing-to-eruption

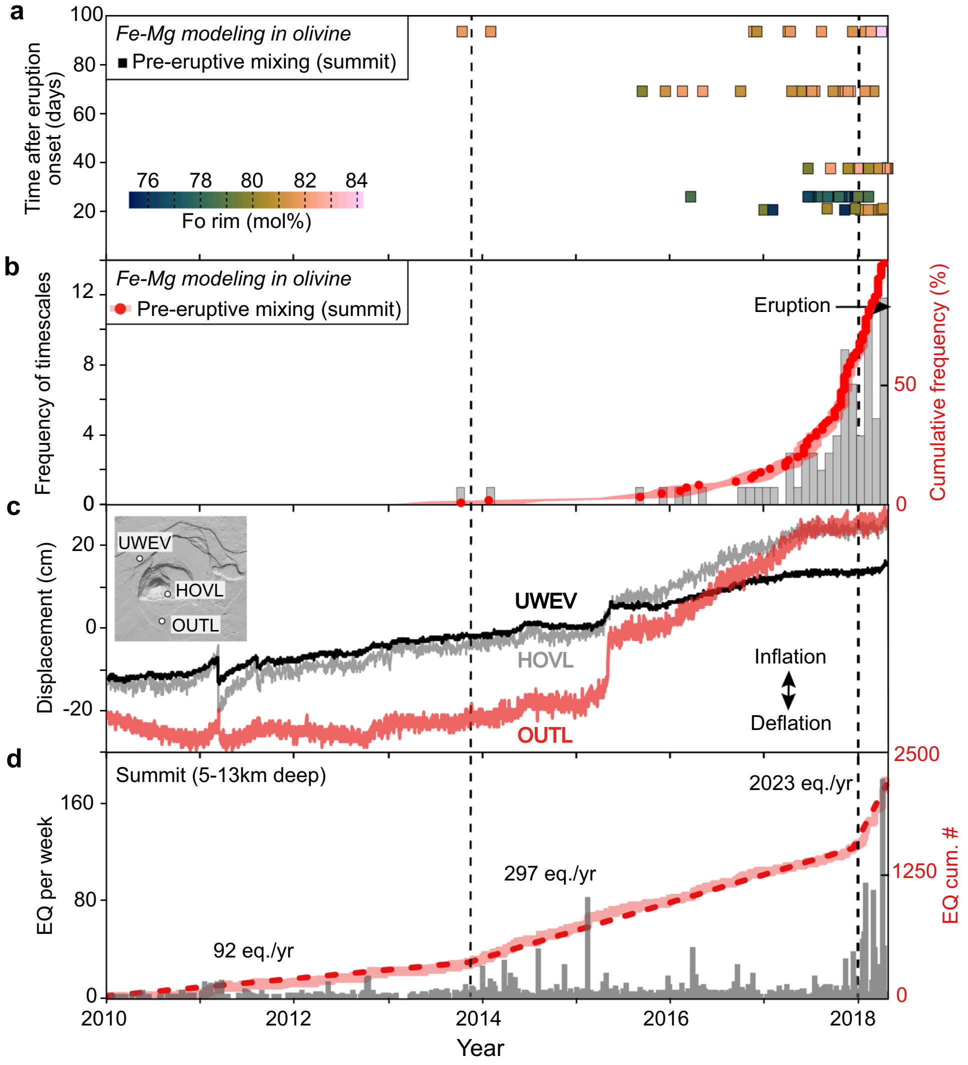

Fig. 7 **Coupling diffusion chronometry to monitoring signals**. **a** Mixing-to-eruption timescales (t_1) vs. the time after eruption onset (in days) on 3 May 2018 for the different samples studied. Symbol colors refer to the Fo rim composition of the olivine. The increase from Fo$_{76–79}$ to Fo$_{82–83}$ in rim compositions over the course of the eruption results from the progressive mixing of the summit melts in equilibrium with Fo$_{80–82}$ with the more evolved melts from the LERZ. **b** Cumulative frequency (red symbols) of mixing-to-eruption timescales extracted from Fe-Mg diffusion chronometry in olivine (the red area is the error bracket associated with the calculated models), and number of crystals per month (histogram). **c** GPS displacement at the summit showing the inflation at the summit between 2010 and April 2018 (UWEV northward component, OUTL vertical component, HOVL vertical component). Note that inflation and deflation signals mainly resolve the behavior of the shallow Halemaʻumaʻu reservoir (Anderson et al. 2019). Inset is a DEM image of the Kīlauea summit with the location of the GPS stations. **d** The 5–13-km-deep seismicity (and EQ cum.#: earthquake cumulative number) measured under the summit show three periods of increasing activity. This depth range is chosen to better resolve seismic activity within the South Caldera reservoir and below. The average number of earthquakes per year was estimated for three time period (1 January 2010–31 December 2014, 1 January 2015–1 January 2018, 2 January 2018–3 May 2018). Taken together, the crystal clock, geodetic, and seismic data reveal that the magma plumbing system at Kīlauea slowly pressurized between 2014 and 2017, a phenomenon that accelerated 6 months before the eruption

times recorded in olivine parallels the ramp-up of deep seismicity recorded 6 months before the eruption (Fig. 7d). Geodetic signals are dominated by deformation of the shallow Halemaʻumaʻu source (Anderson et al. 2019), making it harder to distinguish inflation or deflation at and below the South Caldera reservoir (Fig. 7c). Nevertheless, the GPS stations most adequate to resolve deformation of the shallow Halemaʻumaʻu reservoir (UWEV and HOVL) and the station more likely to detect deformation of the South Caldera reservoir (OUTL) all show inflation after 2014 (Fig. 7c). Hence, the repeated magma intrusions archived in the crystal cargo and the progressive ramp-up of seismicity and deformation together indicate that the volcano was being continuously supplied and priming for a large eruption since at least 2014.

Syn-eruptive mixing in the LERZ

In addition to the pre-eruptive recharges and mixing at the summit, we also find that additional mixing took place directly under the eruption site between summit-derived magma and decade-old LERZ magma pockets. The olivine rim compositions (Fig. 6) in the 2018 LERZ samples support the existence of three different magmas containing melts that were initially in equilibrium with Fo_{84}, $Fo_{80–82}$, and $Fo_{72–77}$ olivine, but progressively changed to melts in equilibrium with a common Fo_{82} olivine composition during the course of the eruption. The low-Fo magma end-member ($Fo_{73–79}$ cores, $Fo_{72–77}$ rims) is likely the old evolved high-Ti basalt stored in the LERZ for decades (Gansecki et al. 2019). Magma with $Fo_{80–82}$ and Fo_{84} olivine from the summit first mixed with the evolved basalt to produce heterogeneous hybrid melts (Fig. 6), which progressively homogenized to melts in equilibrium with Fo_{82} as the more primitive magma became volumetrically dominant during phase 3 of the eruption. Mixing timescales t_2 from Fe-Mg interdiffusion in olivine crystals are on the order of tens of days and thus compatible (97% of $t_2 < 3$ months) with the time for the magma to be transported and mixed with more evolved basalt in the LERZ (Neal et al. 2019). Olivine $>Fo_{82}$ up to Fo_{88} could be part of a mush system that has been under the summit for years (up to centuries; Wieser et al. 2019). Given that the $Fo_{72–77}$ and Fo_{84} end-members rapidly vanished (Fig. 6) and that the summit-derived mafic magma at equilibrium with Fo_{82} olivine accounted for 92–96% of the >1-km^3 erupted magma in 2018 (Neal et al. 2019), the contribution of these magmas was comparatively minor (<8%, based on the proportion of olivine rim compositions with $Fo_{72–77}$ and Fo_{84}). Our syn-eruptive mixing timescales extracted from Fe-Mg interdiffusion in olivine (a few days to months) are similar to those obtained in other basaltic open-vent volcanoes. These have found to be a few hours to days for the 2018 eruption of Ambrym volcano (Moussallam et al. 2021) and days to weeks for Nyiragongo volcano (Connors et al. 2021).

Long-to-medium term priming and short-term triggering of the 2018 Kīlauea eruption

Long-term magma supply variations strongly influence Kīlauea's crustal reservoir system and its eruptive cycles (Poland et al. 2014). Over the past 2500 years, Kīlauea underwent several century-long periods of explosive activity separated by periods of dominantly effusive activity (Swanson et al. 2014). During the last explosive phase (Keanakāko'i Tephra, ~1500–1823 CE), magma supply and eruption rates were low compared to the last 200 years, where Kīlauea activity has been vigorously effusive (Poland et al. 2014; Wright and Klein 2014). During low magma supply explosive periods, magma storage is likely more scattered and transient (Lynn et al. 2017b; Sides et al. 2014), whereas during effusive periods, a steady summit reservoir system is present (Poland et al. 2014). The current effusive period that started in the late eighteenth century (Swanson et al. 2014) saw that average magma supply rates to the summit reservoirs increase from 0.06 to 0.12 km^3/yr between the 1950s and 2018 (Poland et al. 2014; Wright and Klein 2014; Dvorak and Dzurisin 1993). Surges in magma supply spanning a few years in duration have also been detected on top of this general supply rate increase. For instance, the last confirmed major surge occurred between 2003 and 2007 (up to ~0.2 km^3/yr; Poland et al. 2012), corroborated by seismic, deformation, and petrological studies (Thornber et al. 2015; Poland et al. 2012). Similarly, 5–13-km-deep long-period earthquakes in the 6 months preceding the 2018 LERZ eruption were associated with an increase in seismic velocity at the summit and interpreted to signal new magma entering the South Caldera reservoir (Flinders et al. 2020). Subsequently, the entire summit reservoir system became pressurized (Olivier et al. 2019), leading to lava lake overflows and productive earthquake swarms before the collapse of Pu'u'ō'ō on 30 April 2018 (Liu et al. 2018; Chen et al. 2019). The primitive nature of some of 2018 LERZ olivine, as well as the timing of magma intrusion and mixing resolved by diffusion modeling, confirm that physical intrusion of magma at various times prior to May 2018 was a likely cause for runaway pressurization. The two pre-eruptive periods resolved by both cumulative seismicity and crystal clocks are interpreted here as a slow increase in the background magma supply rate (end of 2013 to November 2017), followed by short bursts in magma supply to the South Caldera reservoir (November 2017 to May 2018). The longer (up to 4.5 years) mixing timescales, together with the global inflation at the summit (Fig. 6a–d), are consistent with the summit lava lake overflowing several times between 2014 and May 2018. In a bottom-up scenario, this progressive pressurization of the summit and UERZ prepared Kīlauea Volcano for a major eruption (Swanson et al. 2014).

If subtle increases in magma supply rates in 2014–2018 primed the plumbing system for failure, the exact triggering mechanism that suddenly allowed propagation of magma into the LERZ is harder to ascertain conclusively. One explanation is that the pressurized East Rift Zone system could have reached a critical threshold (Nooner and Chadwick 2016) sufficient to overcome a blockage East of Pu'u'ō'ō that had prevented magma transport downrift since at least 1977 (Neal et al. 2019). Interestingly, while lava levels were rising at Pu'u'ō'ō in the 2 months prior to May 2018, surface flow activity was concurrently decreasing (Orr et al. 2015). Patrick et al. (2020) hypothesized that the short, shallow transport system beneath Puʻuʻōʻō connecting to the surface flows may have been obstructed in the months before the change in activity (Patrick et al. 2019b), ultimately leading to magma back up, and additional pressurization of the UERZ. This finding implies a top-down priming of the eruption, in apparent contradiction with our bottom-up pressurization model. Pre-eruptive seismicity between November 2017 and end April 2018 (see movie M1 in supplementary material) appears to propagate upward from under the South Caldera to the South Caldera and shallow Halemaʻumaʻu region rather than propagate back from Puʻuʻōʻō towards the summit, which might be expected during a top-down pressurization sequence (Roman and Cashman 2018; Tarasewicz et al. 2012). Because the Kīlauea plumbing system was largely open to two vents, however, it is possible that a top-down pressurization (Patrick et al. 2020) could have resulted in little seismicity. Thus, the critical threshold for dike intrusion down to the LERZ may have been attained by the combination of accelerating pressurization associated with increasing magma supply to the South Caldera reservoir and the serendipitous clogging of the small flow-feeding conduit between Puʻuʻōʻō and its satellite vents. We note that while the flank slip associated with the magnitude *M*6.9 earthquake on 4 May 2018 may have opened up the rift zone and heightened flux to the eruption site, it occurred 3 days after magma propagated to the LERZ and therefore cannot be considered a trigger.

Heavy rainfall in the months preceding 3 May was also suggested to have weakened the rift zone, acting as the ultimate eruption trigger without requiring magma input or changes in the pressure state of the plumbing system (Farquharson and Amelung 2020). The study further implied the existence of a correlation between extreme rainfall seasons and eruptions at Kīlauea in the historical record. However, the potential for external forces to prompt the 2018 LERZ Kīlauea eruption is at odds with visual and geodetic observations that indicate a significant increase in magma pressure starting in mid-March 2018, 6 weeks before the eruption (Poland et al. 2022). High ground deformation rates (up to tens of centimeters) and increase of lava lake levels by tens of meters at Puʻuʻōʻō and at the summit before the 2018 eruption, as well as the extension of the ERZ, suggest that the entire Kīlauea magmatic system was pressurized prior to eruption (Patrick et al. 2020; Poland et al. 2022).

To further examine the viability of rainfall as a potential recurring trigger mechanism, we compiled rainfall data and independent information on pre-eruptive tilt and earthquake signals for 49 Kilauea eruptions since 1920 (Fig. 8a–d). Pre-eruptive tilt (inflation) and number of earthquakes (presence/absence of swarms) in the months prior to each eruption are taken here as proxies for eruption causes that are dominantly magmatic. We defined qualitatively four categories of deformation signal (clear inflation, moderate inflation, no inflation, or deflation) and three categories of earthquakes signal (clear earthquake swarm, moderate earthquake, or no earthquake swarm) preceding each eruption since 1920. Rainfall data were surveyed over 1–6 months prior to each eruption. Results show that only 28% of the eruptions had anomalously high rainfall, 39% of the eruptions had normal rainfall, and 33% occurred during an anomalously dry period (Fig. 8b, c, d). In fact, we find that 29 of the 49 Kīlauea eruptions (59%) over the 100-year time series showed 6-month rainfall totals below the period average. Monthly rainfall comparable to end 2017–start 2018 occurs every few years (about once every 3–4 years on average, in the last 50 years). Importantly, there is no significant indication of a relationship between occurrence of high-rainfall periods (n = 30 rainfalls around 2018 levels since 1920, 6 are followed by eruptions <6 months after, for a total of 27 eruptions). Second, to test whether eruptions including 2018 could be associated with rainfall accumulated over longer periods, we compared 6-month total rainfalls prior to 48 individual eruptions and plot them against the total distribution of all 6-month consecutive rainfall totals in the 100-year record (Fig. 8c). A 6-month period was chosen as a maximum definable 'rain season' preceding eruptions and acts to maximize the total rainfall accounted prior to the 2018 eruption, to fall in line with arguments that precipitation was anomalously high (Farquharson and Amelung 2020). Changing this window to 5 months, for instance, reduces the 6-month total by 30% since the November 2017 rainfall was heaviest in this period. Therefore, the analysis of monthly rainfall data between 1920 and 2020 illustrates that there is no clear link between eruption occurrence and heavy rainfall. The 2018 eruption occurred during one of the wettest 6-month period before an eruption (Fig. 8a and c). But without additional evidence for rainfall being a recurring eruption trigger, a causative link remains speculative, and the high pre-2018 rainfall may have been purely coincidental. Instead, analysis of tilt and earthquake records during the same 100-year period (Wright and Klein 2014) clearly demonstrates the link between indicators of magmatic input to the summit or rift system and onset of eruptions. More than 80% of the eruptions that occurred between 1920 and 2020 (n = 49) were preceded by moderate to high inflation and earthquake swarms.

Notwithstanding the ambiguities of interpretation of the final mechanism(s) that lead to the 2018 eruption, the combination of petrological and geophysical data we report supports the priming of the system years in

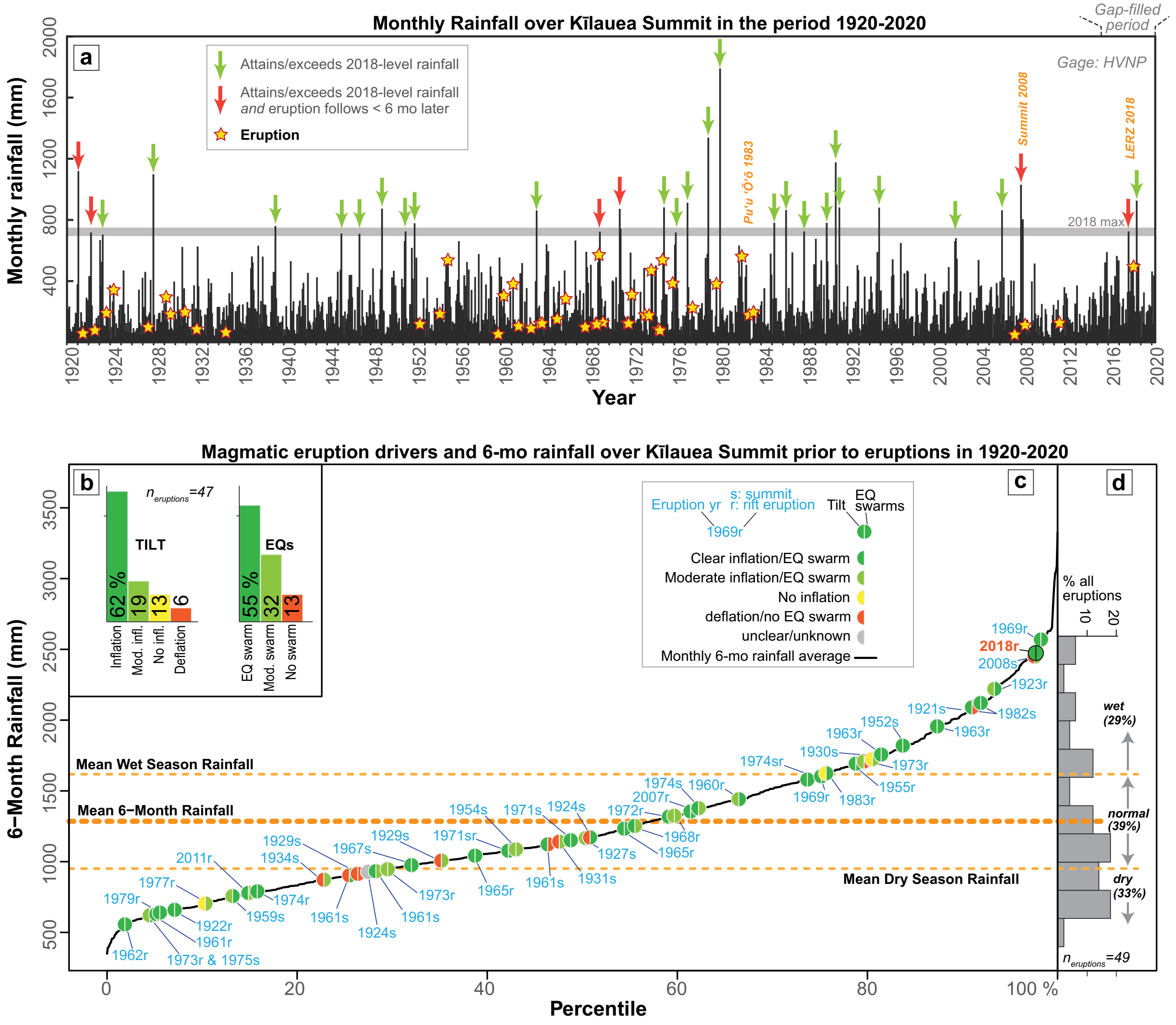

Fig. 8 **Examining correlations between eruptions and rainfall.** **a** Monthly rainfall data for the period 1920–2020 from a rain gage located at the summit of Kīlauea Volcano (Hawai‘i National Volcanoes Park SKN-54). Yellow stars mark the main eruptions over this 100-year period. Green arrows show rainfall months similar in magnitude to 2018, where no eruptions occurred in the 6 months following the rainfall. Red arrows show eruptions that occurred <6 months after a month of heavy rainfall. Grey thick line shows the maximum rainfall in the pre-eruption period in 2018. Note that the maximum monthly rainfall occurs when the eruption is nearly over in August 2018. The 2015–2020 period was gap-filled using neighboring stations (Longman et al. 2020). **b** Pre-eruptive tilt and earthquake (EQ) signals for 47 of 49 Kilauea eruptions since 1920 (data was unavailable for 2 eruptions). Tilt and seismic activity (# of EQ; Wright and Klein 2014) is grouped into four (tilt) and three (EQ) categories to examine the links between typical magmatic signs of unrest (inflation, earthquake swarms) and eruptions. Most eruptions are shortly preceded by magma input into the summit or rift zone system (Wright and Klein 2014). **c** Percentile of 6-month rainfalls that occurred prior to 49 eruptions from 1920 to 2020 (rainfall summed over a period of 6 months before each event). Blue labels show eruption years and location (rift or summit). Symbols are color-coded to show presence or absence of pre-eruptive inflation or EQ swarms. There is no clear tendency for eruptions to occur after any particular amount of 6-month rainfall. **d** Histogram of 6-month rainfall for 49 eruptions, showing that over 1/3 of the eruptions occurred during ‘normal’ rainfall periods (between wet and dry season means), and around 1/3 occurred both during anomalously dry and wet seasons. Therefore, is a random probability that eruptions occur during anomalous rainfall

advance. Such protracted run-up times for magma intrusion and pressurization provide an opportunity to better anticipate these types of eruptions through combinations of physical models of the plumbing system (Anderson and Poland 2016) and exceptional datasets from monitoring networks, and thus could lead to further improvements of hazards assessment and risk mitigation at highly active basaltic shield volcanoes.

Conclusion

In this paper, we address the challenging problem of what processes lead to exceptional eruptions, with the 2018 Kīlauea LERZ eruptive crisis as a case study. By combining timescales obtained by element diffusion in olivine, subsurface seismicity, and edifice deformation, we provide evidence that internal processes (magma recharge under the summit years before the eruption) likely caused the 2018 LERZ eruption. The remarkably well-correlated datasets reveal a slight increase in magma input to the main reservoir around 2014, which accelerated about 6 months prior to May 2018. Bottom-up internal magmatic processes (slow pressurization of the well-supplied magmatic system) were responsible for priming and triggering of the 2018 LERZ Kīlauea eruption rather than external forcings (e.g., anomalously high rainfall). These findings are important for volcanic hazards and for volcano monitoring. Top-down processes such as heavy rainfall and flank sliding are largely unpredictable, whereas the bottom-up symptoms of magma replenishment prior to an eruption that we advocate here can be identified and interpreted months to years in advance.

Supplementary Information The online version contains supplementary material available at https://doi.org/10.1007/s00445-023-01633-4.

Acknowledgements This work is possible thanks to the tireless efforts of the USGS field teams who collected a unique set of samples. We thank Matt Patrick for providing the GPS data and for discussions on the waning activity at Pu‘u‘ō‘ō prior to 2018. We thank the two reviewers, Jordan Lubbers for the U.S. Geological Survey internal review, and the handling editor Matt Patrick for their helpful comments which improved the clarity of the manuscript.

Code availability The codes (and other supplementary materials) used in this study are available on GitHub https://github.com/adrienmourey/BV-2022-Mourey.

Author contributions A. J. M. conceived the study, collected the olivine data, coded the diffusion models, produced the figures, and wrote the manuscript. T. S. contributed to the conceptualization of the study, the diffusion models, the compilation and analysis of rainfall, the interpretations, and manuscript writing and figures. F. C. contributed with writing and discussion of the manuscript. B. S. helped for the interpretation of the seismic data and the discussion. R. J. L. helped for the rainfall data analysis and the discussion.

Funding RAPID Grant from the National Science Foundation (Award #1838502) and NSF EAR Grant (#1725321) were provided to T. S.

Data availability All compositional data obtained in this study are included as supplementary data tables.

Declarations

Competing interests The authors declare no competing interests.

Disclaimer Any use of trade, firm, or product names is for descriptive purposes only and does not imply endorsement by the U.S. Government. Any findings and conclusions or recommendations expressed in this material do not necessarily reflect the views of the National Science Foundation.

References

Albert H, Costa F, Di Muro A, Herrin J, Métrich N, Deloule E (2019) Magma interactions, crystal mush formation, timescales, and unrest during caldera collapse and lateral eruption at ocean island basaltic volcanoes (Piton de la Fournaise, La Réunion). Earth Planet Sci Lett 515:187–199. https://doi.org/10.1016/j.epsl.2019.02.035

Anderson KR, Poland MP (2016) Bayesian estimation of magma supply, storage, and eruption rates using a multiphysical volcano model: Kilauea Volcano, 2000–2012. Earth Planet Sci Lett 447:161–171. https://doi.org/10.1016/j.epsl.2016.04.029

Aubry TJ, Farquharson JI, Rowell CR et al (2022) Impact of climate change on volcanic processes: current understanding and future challenges. Bull Volcanol 84:58. https://doi.org/10.1007/s00445-022-01562-8

Burchardt S, Annen CJ, Kavanagh JL et al (2022) Developments in the study of volcanic and igneous plumbing systems: outstanding problems and new opportunities. Bull Volcanol 84:59. https://doi.org/10.1007/s00445-022-01564-6

Cashman KV, Edmonds M (2019) Mafic glass compositions: a record of magma storage conditions, mixing and ascent. Phil Trans R Soc 377(2139):20180004. https://doi.org/10.1098/rsta.2018.0004

Chakraborty S (2010) Diffusion coefficients in olivine, wadsleyite and ringwoodite. Rev Mineral Geochem 72(1):603–639. https://doi.org/10.2138/rmg.2010.72.13

Chen K, Smith JD, Avouac J-P, Liu Z, Song YT, Gualandi A (2019) Triggering of the M_w 7.2 Hawaii earthquake of May 4, 2018 by a dike intrusion. Geophys Res Lett 46:2503–2510. https://doi.org/10.1029/2018GL081428

Clague DA, Moore JG, Dixon JE, Friesen WB (1995) Petrology of submarine lavas from Kilauea’s Puna Ridge, Hawai‘i. J Petrol 36:299–349. https://doi.org/10.1093/petrology/36.2.299

Connors L, Sublett D, Wallace P, Sims K, Bodnar R (2021) Investigating magma storage histories at flank cones of Nyiragongo and Nyamulagira with olivine-hosted melt inclusions and diffusion chronometry. Am Geophys Union

Coogan LA, Hain A, Stahl S, Chakraborty S (2005) Experimental determination of the diffusion coefficient for calcium in olivine between 900 °C and 1500 °C. Geochem. Cosmochim. Acta 69(14):3683–3694. https://doi.org/10.1016/j.gca.2005.03.002

Cooper KM, Kent AJR (2014) Rapid remobilization of magmatic crystals kept in cold storage. Nature 506(7489):480–483. https://doi.org/10.1038/nature12991

Costa F, Chakraborty S (2004) Decadal time gaps between mafic intrusion and silicic eruption obtained from chemical zoning patterns in olivine. Earth Planet Sci Lett 227(3-4):517–530. https://doi.org/10.1016/j.epsl.2004.08.011

Costa F, Dungan M (2005) Short time scales of magmatic assimilation from diffusion modeling of multiple elements in olivine. Geology 33(10):837–840. https://doi.org/10.1130/g21675.1

Costa F, Dohmen R, Chakraborty S (2008) Time scales of magmatic processes from modeling the zoning patterns of crystals. Rev Mineral Geochem 69(1):545–594. https://doi.org/10.2138/rmg.2008.69.14

Costa F, Shea T, Ubide T (2020) Diffusion chronometry and the timescales of magmatic processes. Nat. Rev. Earth Environ. 1:201–214. https://doi.org/10.1038/s43017-020-0038-x

Danyushevsky LV, Plechov P (2011) Petrolog3: integrated software for modeling crystallization processes. Geochem Geophys Geosyst 12(7):Q07021. https://doi.org/10.1029/2011gc003516

Dietterich HR, Neal CA (2022) A look ahead to the next decade at US volcano observatories. Bull Volcanol 84:63. https://doi.org/10.1007/s00445-022-01567-3

Dohmen R, Chakraborty S (2007) Fe–Mg diffusion in olivine II: point defect chemistry, change of diffusion mechanisms and a model for calculation of diffusion coefficients in natural olivine. Phys Chem Minerals 34(6):409–430. https://doi.org/10.1007/s00269-007-0158-6

Dvorak JJ, Dzurisin D (1993) Variations in magma supply rate at Kilauea Volcano, Hawai'i. J Geophys Res 98:22255–22268. https://doi.org/10.1029/93JB02765

Edmonds M, Sides IR, Maclennan J (2015) Insights into mixing, fractionation and degassing of primitive melts at Kilauea volcano, Hawai'i. In Hawaiian volcanoes: from source to surface. Geophys Mono Series 208:323–349. https://doi.org/10.1002/9781118872079.ch15

Eischeid JK, Pasteris PA, Diaz HF, Plantico MS, Lott NJ (2000) Creating a serially complete, national daily time series of temperature and precipitation for the western United States. J Appl Meteor 39(9):1580–1591.https://doi.org/10.1175/1520-0450(2000)039<1580:cascnd>2.0.co;2

Farquharson JI, Amelung F (2020) Extreme rainfall triggered the 2018 rift eruption at Kilauea Volcano. Nature 580(7804):491–495. https://doi.org/10.1038/s41586-020-2172-5

Flinders AF, Caudron C, Johanson IA, Taira T, Shiro B, Haney M (2020) Seismic velocity variations associated with the 2018 lower East Rift Zone eruption of Kilauea, Hawai'i. Bull. Volcanol 82(6):47. https://doi.org/10.1007/s00445-020-01380-w

Frazier AG, Giambelluca TW, Diaz HF, Needham HL (2016) Comparison of geostatistical approaches to spatially interpolate month-year rainfall for the Hawaiian Islands. Int J Climatol 36(3):1459–1470. https://doi.org/10.1002/joc.4437

Girona T, Costa F (2013) DIPRA: a user-friendly program to model multi-element diffusion in olivine with applications to timescales of magmatic processes. Geochem Geophys Geosys 14(2):422–431. https://doi.org/10.1029/2012gc004427

Gualda GAR, Ghiorso MS, Lemons RV, Carley TL (2012) Rhyolite-MELTS: a modified calibration of MELTS optimized for silica-rich, fluid-bearing magmatic systems. J Petrol 53(5):875–890. https://doi.org/10.1093/petrology/egr080

Gudmundsson A, Drymoni K, Browning J et al (2022) Volcanotectonics: the tectonics and physics of volcanoes and their eruption mechanics. Bull Volcanol 84:72. https://doi.org/10.1007/s00445-022-01582-4

Helz RT, Thornber CR (1987) Geothermometry of Kilauea lki lava lake, Hawaii. Bull Volcanol 49(5):651–668. https://doi.org/10.1007/bf01080357

Helz RT, Cottrell E, Brounce MN, Kelley KA (2017) Olivine-melt relationships and syneruptive redox variations in the 1959 eruption of Kilauea Volcano as revealed by XANES. J Volcanol Geotherm Res 333-334:1–14. https://doi.org/10.1016/j.jvolgeores.2016.12.006

Kress VC, Carmichael ISE (1991) The compressibility of silicate liquids containing Fe_2O_3 and the effect of composition, temperature, oxygen fugacity and pressure on their redox states. Contrib Mineral Petrol 108(1-2):82–92. https://doi.org/10.1007/bf00307328

Lerner AH, Muth MJ, Wallace PJ, Lanzirotti A, Newville M, Gaetani GA, Chowdhury P, Dasgupta R (2021b) Improving the reliability of Fe- and S-XANES measurements in silicate glasses: correcting beam damage and identifying Fe-oxide nanolites in hydrous and anhydrous melt inclusions. Chem Geol 586:120610. https://doi.org/10.1016/j.chemgeo.2021.120610

Liu C, Lay T, Xiong X (2018) Rupture in the 4 May 2018 M_w 6.9 earthquake seaward of the Kilauea east rift zone fissure eruption in Hawaii. Geophys Res Lett 18:9508–9515. https://doi.org/10.1029/2018GL079349

Longman RJ et al (2018) Data descriptor: compilation of climate data from heterogeneous networks across the Hawaiian Islands. Sci Data 5:180012. https://doi.org/10.1038/sdata.2018.12

Longman RJ, Newman AJ, Giambelluca TW, Lucas M (2020) Characterizing the uncertainty and assessing the value of gap-filled daily rainfall data in Hawai'i. J Appl Meteor Climatol 59:1–45. https://doi.org/10.1175/JAMC-D-20-0007.1

Lynn KJ, Garcia MO, Shea T, Costa F, Swanson DA (2017a) Timescales of mixing and storage for Keanakāko'i, tephra magmas (1500–1820 CE), Kilauea volcano, Hawai'i. Contrib Mineral Petrol 172:76–96. https://doi.org/10.1007/s00410-017-1395-4

Lynn KJ, Shea T, Garcia MO (2017b) Nickel variability in Hawaiian olivine: evaluating the relative contribution from mantle and crustal processes. Am Mineral 102:507–518. https://doi.org/10.2138/am-2017-5763

Marshall LR, Maters EC, Schmidt A et al (2022) Volcanic effects on climate: recent advances and future avenues. Bull Volcanol 84:54. https://doi.org/10.1007/s00445-022-01559-3

Matzen AK, Baker MB, Beckett JR, Stolper EM (2013) The temperature and pressure dependence of nickel partitioning between olivine and silicate melt. J Petrol 54(12):2521–2545. https://doi.org/10.1093/petrology/egt055

Mourey AJ, Shea T (2019) Forming olivine phenocrysts in basalt: a 3D characterization of growth rates in laboratory experiments. Front Earth Sci 7:300. https://doi.org/10.3389/feart.2019.00300

Mourey AJ, Shea T, Lynn KJ, Lerner AH, Lambart S, Costa F, Oalmann J, Lopaka Lee R, Gansecki C (2022) Trace elements in olivine fingerprint the source of 2018 magmas and shed light on explosive-effusive eruption cycles at Kilauea Volcano. Earth Planet Sci Lett 595:117769. https://doi.org/10.1016/j.epsl.2022.117769

Moussallam Y, Edmonds M, Scaillet B, Peters N, Gennaro E, Sides I, Oppenheimer C (2016) The impact of degassing on the oxidation state of basaltic magmas: a case study of Kilauea volcano. Earth Planet Sci Lett 450:317–325. https://doi.org/10.1016/j.epsl.2016.06.031

Moussallam Y, Longpré M-A, McCammon C, Gomez-Ulla A, Rose-Koga EF, Scaillet B, Peters N, Gennaro E, Paris R, Oppenheimer C (2019) Mantle plumes are oxidised. Earth Planet Sci Lett 527:115798. https://doi.org/10.1016/j.epsl.2019.115798

Moussallam Y, Médard E, Georgeais G, Rose-Koga EF, Koga KT, Pelletier B, Bani P, Shreve TL, Grandin R, Boichu M (2021) How to turn off a lava lake? A petrological investigation of the 2018 intra-caldera and submarine eruptions of Ambrym volcano. Bull Volcanol 83:1–19. https://doi.org/10.1007/s00445-021-01522-8

Neal CA et al (2019) The 2018 rift eruption and summit collapse of Kilauea volcano. Science 363:367–374. https://doi.org/10.1126/science.aav7046

Newcombe ME, Fabbrizio A, Zhang Y, Ma C, Le Voyer M, Guan Y, Eiler JM, Saal AE, Stolper EM (2014) Chemical zonation in olivine-hosted melt inclusions. Contrib Mineral Petrol 168:1030–1056. https://doi.org/10.1007/s00410-014-1030-6

Nooner SL, Chadwick WW (2016) Inflation-predictable behavior and co-eruption deformation at Axial Seamount. Science 354(6318):1399–1403. https://doi.org/10.1126/science.aah4666

Olivier G, Brenguier F, Carey R, Okubo P, Donaldson C (2019) Decrease in seismic velocity observed prior to the 2018 eruption of Kilauea volcano with ambient seismic noise interferometry. Geophys. Res. Lett. 46:3734–3744. https://doi.org/10.1029/2018gl081609

Orr TR, Poland MP, Patrick MR, Thelen WA, Sutton J, Elias T, Thornber CR, Parcheta C, Wooten KM (2015) Kilauea's 5–9 March 2011 Kamoamoa fissure eruption and its relation to 30+ years of activity from Pu'u 'Ō'ō. Geophys Mono Series 208:393–420. https://doi.org/10.1002/9781118872079.ch18

Patrick MR, Anderson KR, Poland MP, Orr TR, Swanson DA (2015) Lava lake level as a gauge of magma reservoir pressure and eruptive hazard. Geology 43(9):831–834. https://doi.org/10.1130/g36896.1

Patrick M, Orr T, Anderson K, Swanson D (2019b) Eruptions in sync: improved constraints on Kilauea Volcano's hydraulic connection. Earth Planet Sci Lett 507:50–61. https://doi.org/10.1016/j.epsl.2018.11.030

Patrick MR, Houghton BF, Anderson KR et al (2020) The cascading origin of the 2018 Kilauea eruption and implications for future forecasting. Nat. Comm. 11(1):5646. https://doi.org/10.1038/s41467-020-19190-1

Pietruszka AJ, Marske JP, Heaton DE, Garcia MO, Rhodes M (2018) An isotopic perspective into the magmatic evolution and architecture of the rift zones of Kilauea volcano. J Petrol 59:2311–2352. https://doi.org/10.1093/petrology/egy098

Pietruszka AJ, Garcia MO, Rhodes JM (2021) Accumulated Pu'u 'Ō'ō magma fed the voluminous 2018 rift eruption of Kilauea Volcano: evidence from lava chemistry. Bull Volcanol 83:59. https://doi.org/10.1007/s00445-021-01470-3

Poland MP, Miklius A, Jeff Sutton A, Thornber CR (2012) A mantle-driven surge in magma supply to Kilauea Volcano during 2003–2007. Nat Geosc 5(4):295–300. https://doi.org/10.1038/ngeo1426

Poland MP, Miklius A, Montgomery-Brown EK (2014) Magma supply, storage, and transport at shield-stage Hawaiian volcanoes. USGS Surv. Prof. Pap. 1801:179–234. https://doi.org/10.3133/pp18015

Poland MP, Hurwitz S, Kauahikaua JP et al (2022) Rainfall an unlikely factor in Kilauea's 2018 rift eruption. Nature 602:E7–E10. https://doi.org/10.1038/s41586-021-04163-1

Putirka KD (2008) Thermometers and barometers for volcanic systems. Rev Mineral Geochem 69(1):61–120. https://doi.org/10.2138/rmg.2008.69.3

Putirka K (2016) Rates and styles of planetary cooling on Earth, Moon, Mars, and Vesta, using new models for oxygen fugacity, ferric-ferrous ratios, olivine-liquid Fe-Mg exchange, and mantle potential temperature. Am Mineral 101(4):819–840. https://doi.org/10.2138/am-2016-5402

Roman DC, Cashman KV (2006) The origin of volcano-tectonic earthquake swarms. Geology 34:457–460. https://doi.org/10.1130/G22269.1

Roman DC, Cashman KV (2018) Top-down precursory volcanic seismicity: implications for 'stealth' magma ascent and long-term eruption forecasting. Front Earth Sci 6:124. https://doi.org/10.3389/feart.2018.00124

Ruprecht P, Plank T (2013) Feeding andesitic eruptions with a high-speed connection from the mantle. Nature 500(7460):68–72. https://doi.org/10.1038/nature12342

Ruth DCS, Costa F, Bouvet de Maisonneuve C, Franco L, Cortés JA, Calder ES (2018) Crystal and melt inclusion timescales reveal the evolution of magma migration before eruption. Nat Comm 9(1):2657. https://doi.org/10.1038/s41467-018-05086-8

Schmincke HU (2004) Volcanism. Springer, Berlin. https://doi.org/10.1007/978-3-642-18952-4

Shea T, Costa F, Krimer D, Hammer JE (2015a) Accuracy of timescales retrieved from diffusion modeling in olivine: a 3D perspective. Am Mineral 100(10):2026–2042. https://doi.org/10.2138/am-2015-5163

Shea T, Lynn KJ, Garcia MO (2015b) Cracking the olivine zoning code: distinguishing between crystal growth and diffusion. Geology 43(10):935–938. https://doi.org/10.1130/g37082.1

Sides IR, Edmonds M, Maclennan J, Swanson DA, Houghton BF (2014) Eruption style at Kilauea Volcano in Hawai'i linked to primary melt composition. Nat Geosc 7(6):464–469. https://doi.org/10.1038/ngeo2140

Sigmundsson F (2019) Calderas collapse as magma flows into rifts. Science 366:1200–1201. https://doi.org/10.1126/science.aaz7126

Sigvaldason GE, Annertz K, Nilsson M (1992) Effect of glacier loading/deloading on volcanism: postglacial volcanic production rate of the Dyngjufjöll area, central Iceland. Bull Volcanol 54(5):385–392. https://doi.org/10.1007/bf00312320

Sparks RSJ (2003) Forecasting volcanic eruptions. Earth Planet Sci Lett 210:1–15. https://doi.org/10.1016/S0012-821X(03)00124-9

Swanson DA, Rose TR, Mucek AE, Garcia MO, Fiske RS, Mastin LG (2014) Cycles of explosive and effusive eruptions at Kilauea Volcano, Hawai'i. Geology 42(7):631–634. https://doi.org/10.1130/g35701.1

Tarasewicz J, White RS, Woods AW, Brandsdóttir B, Gudmundsson MT (2012) Magma mobilization by downward-propagating decompression of the Eyjafjallajökull volcanic plumbing system. Geophys Res Lett 39(19):L19309. https://doi.org/10.1029/2012gl053518

Thomson A, Maclennan J (2013) The distribution of olivine compositions in Icelandic basalts and picrites. J Petrol 54(4):745–768. https://doi.org/10.1093/petrology/egs083

Thornber CR, Orr TR, Heliker C, Hoblitt RP (2015) Petrologic testament to changes in shallow magma storage and transport during 30+ years of recharge and eruption at Kilauea volcano, Hawai'i. USGS Surv. Prof. Pap 208:147–188. https://doi.org/10.1002/9781118872079.ch8

Wech AG, Thelen WA (2015) Linking magma transport structures at Kilauea volcano. Geophys Res Lett 42:7090–7097. https://doi.org/10.1002/2015gl064869

Wieser PE et al (2019) Crystal scavenging from mush piles recorded by melt inclusions. Nat. Comm 10(1):5797. https://doi.org/10.1038/s41467-019-13518-2

Wieser PE, Edmonds M, Gansecki C et al (2022) Explosive activity on Kilauea's lower East Rift zone fueled by a volatilerich, Dacitic Melt. Geochem Geophys Geosyst 23:e2021GC010046. https://doi.org/10.1029/2021GC010046

Wright TL, Klein FW (2014) Two hundred years of magma transport and storage at Kilauea Volcano, Hawai'i, 1790–2008. U.S. Geol Surv Prof Pap 1806:1–240. https://doi.org/10.3133/pp1806

Zolotov MY, Fegley B (1999) Oxidation state of volcanic gases and the interior of Io. Icarus 141(1):40–52. https://doi.org/10.1006/icar.1999.6164

Anderson KR et al (2019) Magma reservoir failure and the onset of caldera collapse at Kilauea Volcano in 2018. Science 366(6470). https://doi.org/10.1126/science.aaz1822

Dietterich H, Diefenbach A, Soule S, Zoeller M, Patrick M, Major J, Lundgren P (2021) Lava effusion rate evolution and erupted volume during the 2018 Kilauea lower East Rift Zone eruption. Bull Volcanol 83(25). https://doi.org/10.1007/s00445-021-01443-6

Gansecki C et al (2019) The tangled tale of Kilauea's 2018 eruption as told by geochemical monitoring. Science 366(6470). https://doi.org/10.1126/science.aaz0147

Gordeychik B, Churikova T, Shea T, Kronz A, Simakin A, Wörner G (2020) Fo and Ni relations in olivine differentiate between crystallization and diffusion trends. J Petrol 61. https://doi.org/10.1093/petrology/egaa083

Lerner AH, Wallace PJ, Shea T, Mourey AJ et al (2021a) The petrologic and degassing behavior of sulfur and other magmatic volatiles from the 2018 eruption of Kilauea, Hawai'i: melt concentrations, magma storage depths, and magma recycling. Bull Volcanol 83(6). https://doi.org/10.1007/s00445-021-01459-y

Mourey AJ, Shea T, Hammer JE (2023) Preservation of magma recharge signatures in Kilauea olivine during protracted storage. J Geophys Res: Solid Earth e2022JB025523. https://doi.org/10.1029/2022JB025523

Patrick MR et al (2019a) Cyclic lava effusion during the 2018 eruption of Kilauea Volcano. Science 366(6470). https://doi.org/10.1126/science.aay9070

Shea T, Matzen AK, Mourey AJ (2022) Experimental study of Fe–Mg partitioning and zoning during rapid growth of olivine in Hawaiian tholeiites. Contrib Mineral Petrol 177(114). https://doi.org/10.1007/s00410-022-01969-8

Wieser PE et al (2021) Reconstructing magma storage depths for the 2018 Kīlauean eruption from melt inclusion CO_2 contents: the importance of vapor bubbles. Geochem Geophys Geosyst 22(2). https://doi.org/10.1029/2020gc009364